Investigation of coarsening of oxide nanoparticles at 1400 K and its effect on the microstructure formation of an ODS Eurofer steel

Marques Pereira, V.; Davis, T. P.; Mayoral, M. H.; Kumar, A.; Schut, H.; Sietsma, J.

Important note
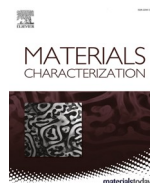To cite this publication, please use the final published version (if applicable).
Please check the document version above.

Investigation of coarsening of oxide nanoparticles at 1400 K and its effect on the microstructure formation of an ODS Eurofer steel

V.S.M. Pereira [a,b,*], T.P. Davis [c,1], M.H. Mayoral [d], A. Kumar [a,2], H. Schut [b], J. Sietsma [a]

[a] Delft University of Technology, Department of Materials Science and Engineering, Faculty of Mechanical, Maritime and Materials Engineering. Mekelweg 2, 2628CD Delft, the Netherlands
[b] Delft University of Technology, Department of Radiation Science and Technology, Faculty of Applied Sciences. Mekelweg 15, 2629JB Delft, the Netherlands
[c] University of Oxford, Department of Materials, Parks Road, OX1 3PH Oxford, United Kingdom
[d] CIEMAT, Department of Technology, Division of Materials of Energy Interest. Complutense Avenue, 40, 28040 Madrid, Spain

ARTICLE INFO

ABSTRACT

Oxide Dispersion Strengthened (ODS) steels are potential candidate materials for application as structural components of fission and fusion reactors, known for their high thermal stability, high resistance to creep and to radiation-induced damage. These attractive properties result from the presence of the fine and highly thermally stable yttrium-oxygen (Y-O) based nanoparticles, which exert a strong Zener pinning force to hinder the grain boundary movement, and are able to pin dislocations and trap radiation induced defects. In the present work, the effect of annealing at 1400 K on the microstructure and oxide nanoparticles in a 0.3% Y_2O_3 ODS Eurofer steel was assessed. The material was characterized with Scanning Electron Microscopy, Transmission Electron Microscopy and Atom Probe Tomography in a reference condition and after annealing at 1400 K, followed by cooling at different rates. The results showed that the average diameter of the oxide nanoparticles increases from 3.7 ± 0.01 nm to 5.3 ± 0.04 nm, after annealing at 1400 K for 1 h. The particles present a well-known core/shell structure, with a core rich in Y, O and V and a shell rich in Cr. The effect of the increase in oxide nanoparticle size on the microstructure is discussed in terms of the Zener pinning force.

1. Introduction

Oxide Dispersion Strengthened (ODS) steels have been developed and extensively researched in the past decades due to their potential for application as structural components in nuclear fission and fusion reactors [1,2]. The oxide nanoparticles dispersed in the matrix, with typical particle size varying from 3 nm to 20 nm [3], are able to pin dislocations and hinder grain boundary movement; the particles can also act as efficient trapping sites for radiation-induced damage. The matrix of ODS steels is commonly ferritic (Cr content higher than 12 wt%), or composed of mixture of tempered martensite and ferrite (9–10 wt% Cr). Therefore, ODS steels present high tensile strength, good ductility and, most importantly, high thermal stability of the microstructure, high resistance to creep and improved resistance to radiation-induced embrittlement. [4,5]

Yttrium oxide (Y_2O_3) is the type of oxide that is most commonly used

in ODS steels because of its high thermal stability and, consequently, for providing superior mechanical properties, in comparison to other types of oxides [6,7]. The Y_2O_3 particles are incorporated by mechanical alloying with the metallic powders of the alloying elements to constitute the steel. During this process, the Y_2O_3 particles initially in powder form dissolve in the matrix and, only during the subsequent fabrication steps, they re-precipitate in the form of Y-O based nanoparticles. The chemical composition and crystal structure of the precipitated nanoparticles depend on the alloying elements present in the material and on the processing parameters. Y-O based nanoparticles have been reported by several authors to be highly thermally stable. Zilnyk et al. [6] did not observe any significant alteration in Y-O based particles dispersed in an ODS Eurofer steel after annealing at 1073 K for 6 months. The coarsening of Y-O based particles in ODS Eurofer has been observed only after annealing at the range 1500–1600 K, which leads also to the overall coarsening of the microstructure [8,9]. The high stability of fine Y-O

based nanoparticles is attributed to a high coherency of the interface of the particle with the ferrite matrix, which results in a small driving force for coarsening, and the low solubility of Y and O in Fe [4,6,10].

Nevertheless, in a previous study [11] significant instability of the microstructure of an 0.3% Y_2O_3 ODS Eurofer steel was observed after annealing at 1400 K for 1 h. Upon moderate cooling to room temperature, a high volume fraction of recrystallized ferrite was formed, accompanied by lath martensite and equiaxed martensite. The described microstructure contradicts Thermo-Calc predictions for the steel, which should be austenitic at 1400 K [11], and observations made by other authors [9,12]. A possible explanation for the microstructure described in [11] is that a fraction of the Y-O based nanoparticles in the particular steel go through coarsening during annealing at 1400 K, reducing the Zener pinning force. In the present work, we investigate the possible coarsening of Y-O nanoparticles present in the 0.3% Y_2O_3 ODS Eurofer, after annealing at 1400 K. In addition, the oxide nanoparticles are characterized with Transmission Electron Microscopy and Atom Probe Tomography.

2. Experimental

2.1. Materials

The material studied is the 0.3% Y_2O_3 ODS Eurofer steel, produced by conventional powder metallurgy route (mechanical alloying, HIP and thermomechanical treatments) and previously characterized in [11]. Its simplified chemical composition, in weight percent, is Fe-0.1C-9Cr-1 W-0.2 V-0.4Mn-0.3Y_2O_3. The material goes through austenitic transformation, with $A_{c1} = 1152$ K, $A_{c3} = 1187$ K and $M_s = 674$ K, determined by dilatometry [11]. According to ThermoCalc calculations, the steel should be fully austenitic between ~1170 K and ~ 1500 K; between 1500 and ~ 1650 K, the material should be formed by austenite and delta ferrite (Fig. 1). The equilibrium phases displayed in Fig. 1 have been characterized by Pereira et al. [11] and could form during the performed heat treatments, as described below.

In the present work, the 0.3% Y_2O_3 ODS Eurofer steel is analysed in the reference state and annealed at 1400 K for 1 h. A reference state was created in order to obtain a microstructure composed of tempered martensite and $M_{23}C_6$ precipitates, common in ODS Eurofer steels, which provides good mechanical strength and ductility. Hence, the reference state was created by: (i) austenitizing the material at 1253 K for 0.5 h, (ii) cooling to room temperature (formation of martensite), (iii) tempering at 1033 K for 1.5 h and (iv) final cooling to room temperature. All heat treatments were performed in a resistance heating furnace, under a pressure of 10^{-7} mbar. The cooling of steps (ii) and (iv) was done inside the furnace, by switching off its power supply. The average cooling rate thus induced had an exponential character, with an average value of 0.5 K.s^{-1} between 1050 K and 750 K, which is a temperature range critical for phase transformations. Subsequently, further annealing at 1400 K for 1 h was performed in the same conditions. More details about the chemical composition of the steel, dilatometry and the heat treatments in the resistance heating furnace are described in [11]. In order to evaluate the effect of the cooling rate on the microstructure, an extra condition was created. It consisted of 1 h annealing at 1400 K, in a tubular furnace, under N_2 atmosphere, and cooling to room temperature by water quench. This sample is referred as 1400 K-WQ and the sample cooled inside the furnace is referred as 1400 K-FC.

2.2. Methods

The overall microstructure of the 0.3% Y_2O_3 ODS Eurofer steel in its reference state and after annealing at 1400 K (1400 K-FC and 1400 K-WQ) was evaluated using Scanning Electron Microscopy (SEM) and Vickers hardness. The microscope used for SEM analysis was a JEOL 6500FD microscope and the samples were etched with Kallings' 1. For the Vickers Hardness measurements, a load of 0.3 kgf in a Struers Durascan 70 device was used.

Transmission Electron Microscopy (TEM) and Atom Probe Tomography (APT) analyses were carried out to characterize the Y-O based nanoparticles in the reference state and 1400 K-FC. The samples for TEM examination were in the form of discs with 3 mm diameter, punched out from 0.3 mm thick plates. Mechanical polishing of the discs was performed to reach a final thickness of 0.1 mm. Finally, electropolishing in a Tenupol 5 machine with a mixture of 5% perchloric acid and methanol, at 213 K (−60 °C), was performed to reach electron transparency. TEM examination was carried out using standard imaging methods of Bright Field (BF) and Weak Beam Dark Field (WBDF) in a TEM JEOL JEM-2100, with LaB$_6$ filament and operating at 200 keV, available at the National Centre of Electron Microscopy (CNME), Madrid, Spain. Furthermore, STEM mode analysis was applied in both High-Angle Annular Dark Field (HAADF) and BF modes in the Talos Field Emission Gun TEM/STEM, available at the Institute of Madrid for Advanced Studies in Materials (IMDEA), Madrid, Spain. Compositional maps of areas observed with TEM were obtained using Energy Dispersive Spectroscopy (EDS).

Quantitative analyses of the TEM images were done using the software *ImageJ 1.53c,* in order to determine the size distribution and to estimate the number density of the Y-O based nanoparticles. For the calculation of size distributions, the particles are approximated as spheres and, thus, the particle size is given as the diameter. A total of 1887 particles were measured for each analysed condition. The number density of particles corresponds to the number of particles counted in different TEM images per unit volume. A total of 6 images per condition were measured, and the thickness of the TEM samples was assumed to be 100 nm (the actual thickness of the sample could not be experimentally measured).

The APT specimens were first bulk-milled by Focused Ion Beam (FIB)-milling in a dual-beam Helios GE UXe SEM/FIB, located at the Department of Materials Science and Engineering, Delft University of Technology. Final cleaning of the specimens was performed using 2 kV Ga ions in a Zeiss Crossbeam 540 Analytical FIB-SEM at the Department of Materials, University of Oxford. The APT analyses were conducted with a CAMECA LEAP® 5000XR instrument, also at the Department of
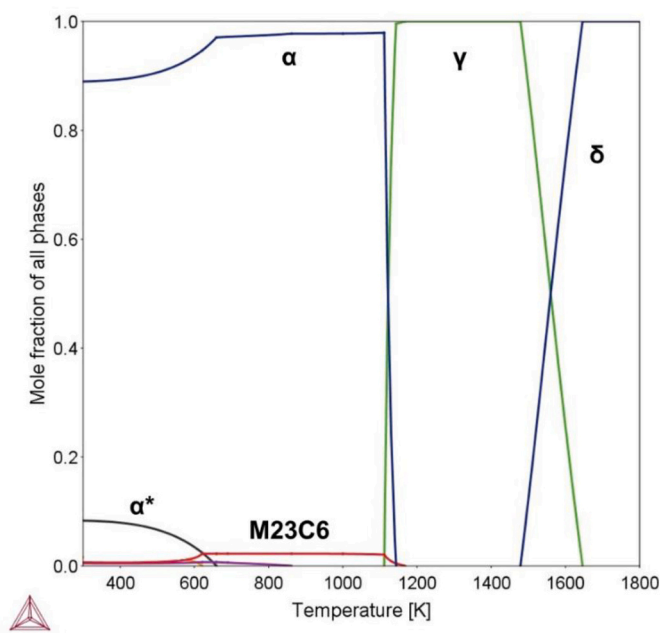

Fig. 1. Mole fraction of phases that can be present in the 0.3% Y_2O_3 ODS Eurofer steel, calculated for its composition without the oxide particles. Composition used: Fe-0.1C-9.18Cr-1.97 W-0.196 V; Thermo-Calc version and database: 2018a and TCFE9 Steels/Fe-alloys v9.0.

Materials from the University of Oxford. The atom probe tips were cooled down and maintained at 55 K. The APT measurements were made in laser mode, under ultra-high vacuum, with a frequency tripled Nd:YAG laser, with 355 nm wave-length, operating at 40 pJ and 200 kHz. The average detection rate was of 1.0% and the detection efficiency of the LEAP 5000XR is 52% [13]. The 3D reconstructions of chemical atomic maps and overall data analysis were made with the software CAMECA IVAS® 3.8.4. Characterization of any overlapping peaks was made using the tool "Peak Decomposition analysis" of IVAS. With this tool, ions can be assigned to overlapping peaks by comparing their decomposed abundance with their expected abundance. Information about the oxide nanoparticles, like chemical composition, size distribution and number density were obtained using the tool "Cluster Analysis" of IVAS and following a maximum separation method, as conducted by Davis et al. [14]. The method is described in detail by Vaumousse et al. [15]. The parameters used for the cluster analysis were refined for each data set, to maximise the accuracy of detection of the nanoparticles. An extra practice was carried out, to verify the suitability of the parameters determined by the maximum separation method. It consists of comparing APT reconstructions containing, separately, only matrix atoms and solute/clusters atoms (obtained after cluster analysis) with the original reconstructions (obtained prior to cluster analysis) and verifying the correct identification of precipitates. Table 1 summarizes the range of parameters and types of ions used in the cluster analyses of oxide nanoparticles in the reference state and annealed at 1400 K.

3. Results

3.1. Characterization of oxide nanoparticles in the reference state and after annealing at 1400 K

Figs. 2(a) and 2(b) contain secondary electrons micrographs of the samples 1400 K-FC and 1400 K-WQ, respectively; Fig. 2(c) shows the microstructure in the reference state. The average Vickers hardness measured in each condition is also shown. Figs. 2(d) and 2(d1) contain bright-field TEM micrographs of the sample 1400 K-FC, showing in more detail the microstructure composed of coarse recrystallized ferrite (light grey, deformation-free grains) and martensite (dark regions). In Fig. 2 (e), the microstructure in the reference state is shown for comparison.

In the reference state the material contains tempered martensite, retained ferrite and $M_{23}C_6$ carbides (indicated by red arrows in Fig. 2 (c)). The retained ferrite corresponds to a fraction of ferrite that does not transform into austenite at temperatures above A_{c3}, due to the pinning of the α/γ interface by Y-O based nanoparticles [16–18]. The retained ferrite can be distinguished from the recrystallized ferrite by its rough, deformed aspect (the deformed state is originated during fabrication of the material). According to Thermo-Calc calculations shown in Fig. 1, the equilibrium phase at 1400 K should be austenite and, considering the effect of oxide nanoparticles, the expected microstructure upon cooling to room temperature should be similar to the one described for the reference state, but without the $M_{23}C_6$ carbides. However, it is seen in Figs. 2(a) and (d) a mixture of coarse recrystallized ferrite, martensite laths and equiaxed nanosized martensite. The microstructure of sample 1400 K-WQ contains also grains of recrystallized ferrite, indicated in Fig. 2(b), surrounded by areas of a rough aspect. It has been seen in the characterization of the matrix with EBSD [11] that these rough areas

correspond to nanosized equiaxed martensite, which are completely corroded during etching. The Vickers hardness values measured after annealing at 1400 K are lower than in the reference state, in agreement with the coarser and partially recrystallized microstructure formed. The grain size distributions of the material in the reference state and after annealing at 1400 K can be found in [11]; the average grain size in the reference state is 0.7 ± 0.5 μm and in the annealed condition is 1.0 ± 1.1 μm (high standard deviation due to heterogeneity of microstructure). In addition, the Vickers hardness measured in the sample 1400 K-WQ is very heterogeneous, as indicated by its high standard deviation. Some regions of the samples present hardness of ~400 HV and others have hardness of ~310 HV.

Figs. 3(a) and (b) show the Y-O based nanoparticles in the reference state, Figs. 3(c-e) show the particles in the material annealed at 1400 K-FC. It is possible to see in Figs. 3(a-e) that the particle size is not homogeneous in any of the cases and examination of different regions of the samples indicate that the particles can be found either inside grains or adjacent to grain boundaries – no preferential disposition of oxide nanoparticles along microstructural features is observed. Fig. 3(c) shows regions with low density of oxide nanoparticles and in Fig. 3(d), a small band free of oxide nanoparticles can be seen encircled in red.

APT analyses were performed on multiple samples taken from different regions of the microstructure, some containing multiple nanosized grains, others taken from larger, micrometric grains. Attention was paid to possible overlapping peaks in the APT mass spectra. In the APT spectra, overlapping of peaks was only observed in the range from 24.87 Da to 25.37 Da, which could be assigned to Cr^{2+} and V^{2+}. For the ion Cr^{2+}, peak decomposition analysis shows a decomposed abundance of 3.28% and expected abundance of 4.35%, with a 0.01% error. For the V^{2+} ion, the decomposed and expected abundance are, respectively, 6.91% and 0.25%, with an error of 1.02%. Based on these results, the peak at 24.87–25.37 Da was assigned to Cr^{2+}. Fig. 4 contains 3D reconstructions of representative tips in the reference state and annealed at 1400 K-FC. In order to visualize the distribution of atoms and ions throughout the tips, and to have qualitative information about the composition of the tips, the reconstructions are given in the form of elemental maps. The reconstructions of Fig. 4(a), of a tip in the reference state, presents two ferrite grains, part of an $M_{23}C_6$ carbide (bottom of the tip) and oxide nanoparticles evenly distributed. The $M_{23}C_6$ carbide is rich in Cr, W and V, in agreement with EDS analysis presented in [11]; a low concentration of Mn is also observed in the carbide. The oxide nanoparticles are rich in Y, V and O, which were also detected in the form of the complex ions VO^{2+} and YO^{2+}. CrO^{2+} and VN^{2+} ions are also present in the oxide nanoparticles, however, due to their significantly lower contents, maps with these ions are not shown. In Fig. 4(b), the reconstruction of the tip taken from the annealed sample shows oxide nanoparticles of various sizes, one of them with ~50 nm length. Qualitatively, the surrounding matrix is enriched with Cr, W, V, likely due to the dissolution of $M_{23}C_6$ carbides during the annealing treatment. In comparison to the reference state, the contents of Y and O, in particular around the coarser particles, are also higher in the matrix. In addition, the coarser oxide particles appear enriched with Si. X-ray Fluorescence analysis of the 0.3% Y_2O_3 ODS Eurofer steel, described in [11], showed that Ta was found in trace amounts within the steel's composition. Ta was not found in any of the APT tips measured, thus, confirming the X-Ray Fluorescence chemical analysis.

Table 1
Parameters used in the cluster analysis with IVAS, determined with the maximum separation method.

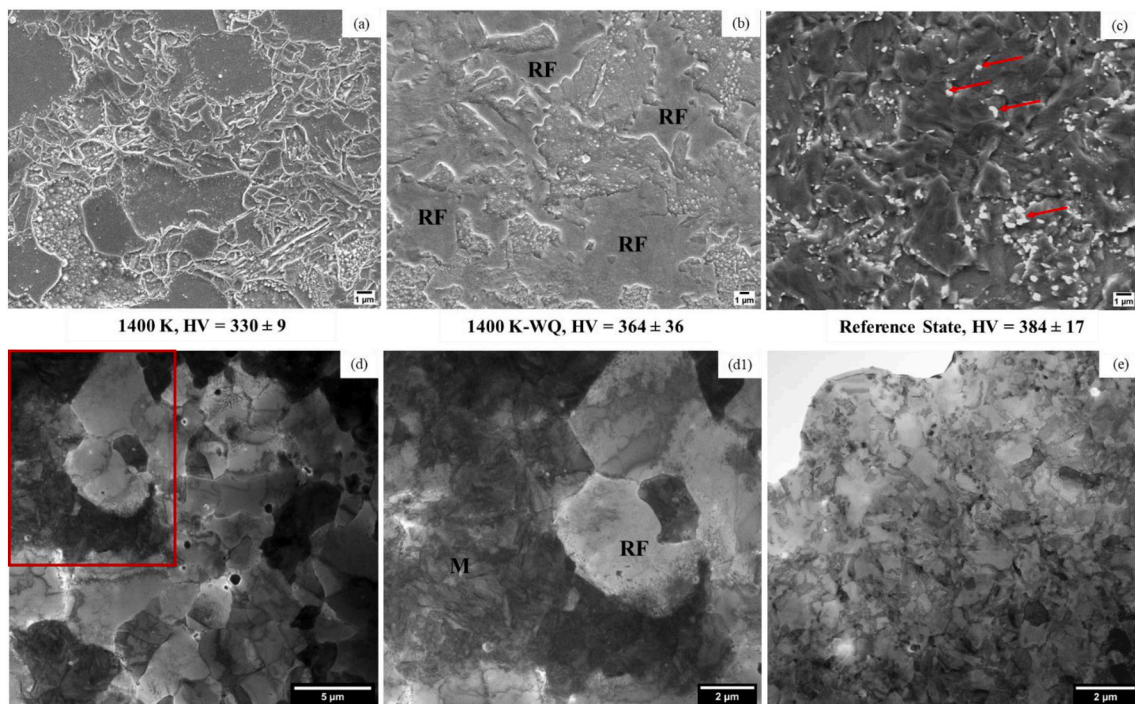|	Ions	KNN (order of nearest neighbour distribution)	N_{min}, atoms (minimum critical size of cluster)	d_{max}, nm (maximum distance between atoms in a detected cluster)	d_e, nm (erosion)	L, nm (envelope)
Reference state	Y, O, V, YO^{2+}, VO^{2+}	1 to 3	5 to 22	0.8 to 1.1	0.4 to 0.55	0.4 to 0.55
1400 K-FC	Y, VO^{2+}, YO^{2+}	1 to 3	6 to 10	0.8 to 1.0	0.4 to 0.5	0.4 to 0.5

Fig. 2. Secondary electron micrographs of the 0.3% Y_2O_3 ODS Eurofer steel and respective average Vickers hardness in the (a) condition of annealing at 1400 K, followed by furnace cooling (1400 K-FC), (b) annealed at 1400 K and water quenched (1400 K-WQ) and (c) reference state, with red arrows indicating $M_{23}C_6$ carbides. (d) and (d1) Bright-field micrographs showing the martensite (M) and recrystallized ferrite (RF) in the sample 1400 K-FC and (e) reference state. (For interpretation of the references to colour in this figure legend, the reader is referred to the web version of this article.)
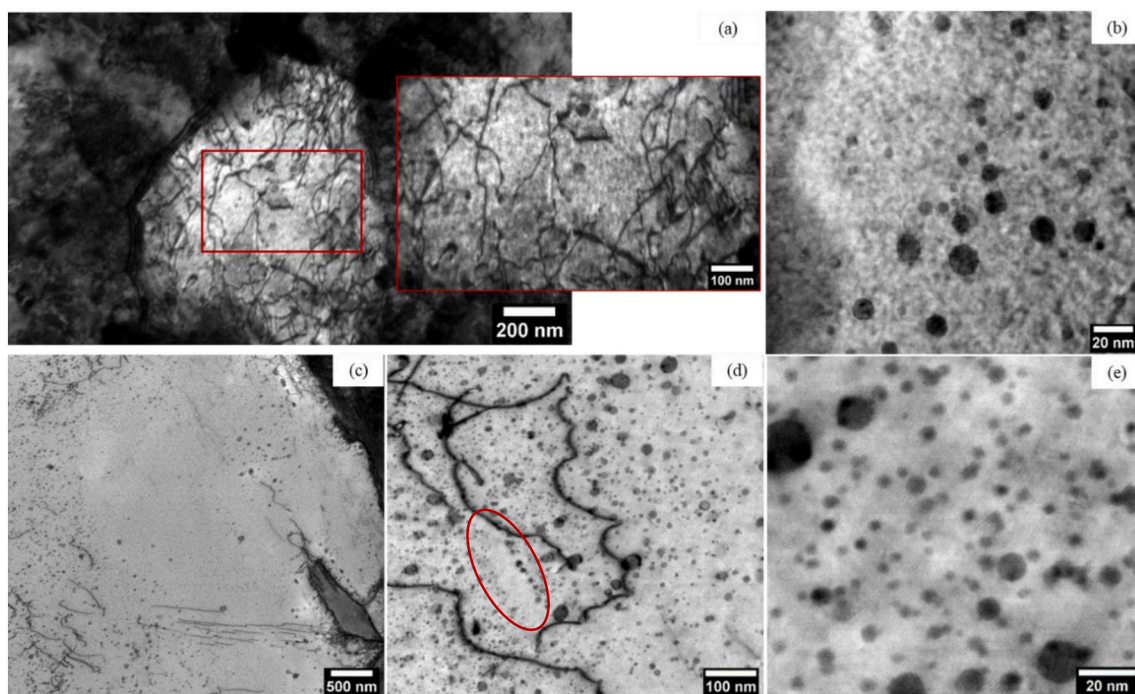

Fig. 3. Bright-field micrographs of the 0.3% Y_2O_3 ODS Eurofer showing Y-O based nanoparticles and their distribution in the matrix. In (a) and (b) the material is in the reference state and in (c), (d) and (e) in the condition 1400 K-FC. In (d), a band free of oxide nanoparticles is encircled in red. (For interpretation of the references to colour in this figure legend, the reader is referred to the web version of this article.)

Quantitative information about the chemical composition of the oxide nanoparticles, size distribution and number density were obtained after performing the cluster analysis, as described in section 2.2. The size distribution and the number density of particles were also calculated using TEM micrographs. These two techniques have certain limitations, but their combined use is able to give complementary information about the material. TEM can be considered a more appropriate tool for determination of particle size distribution and for general observation of
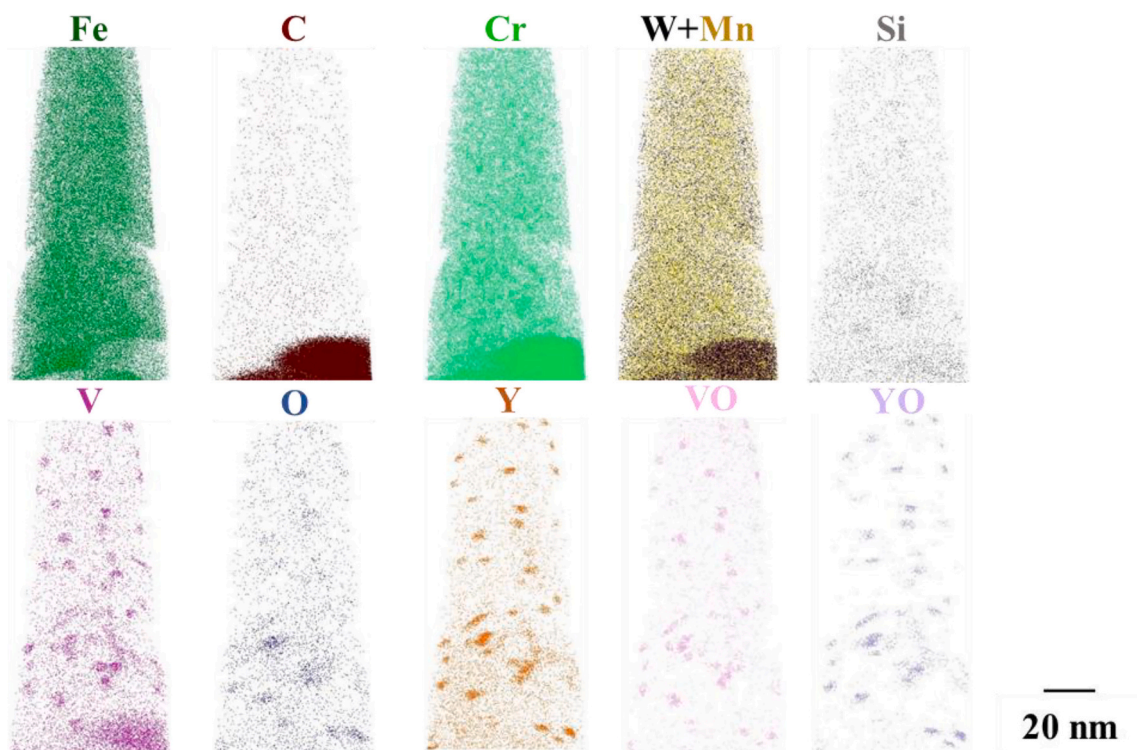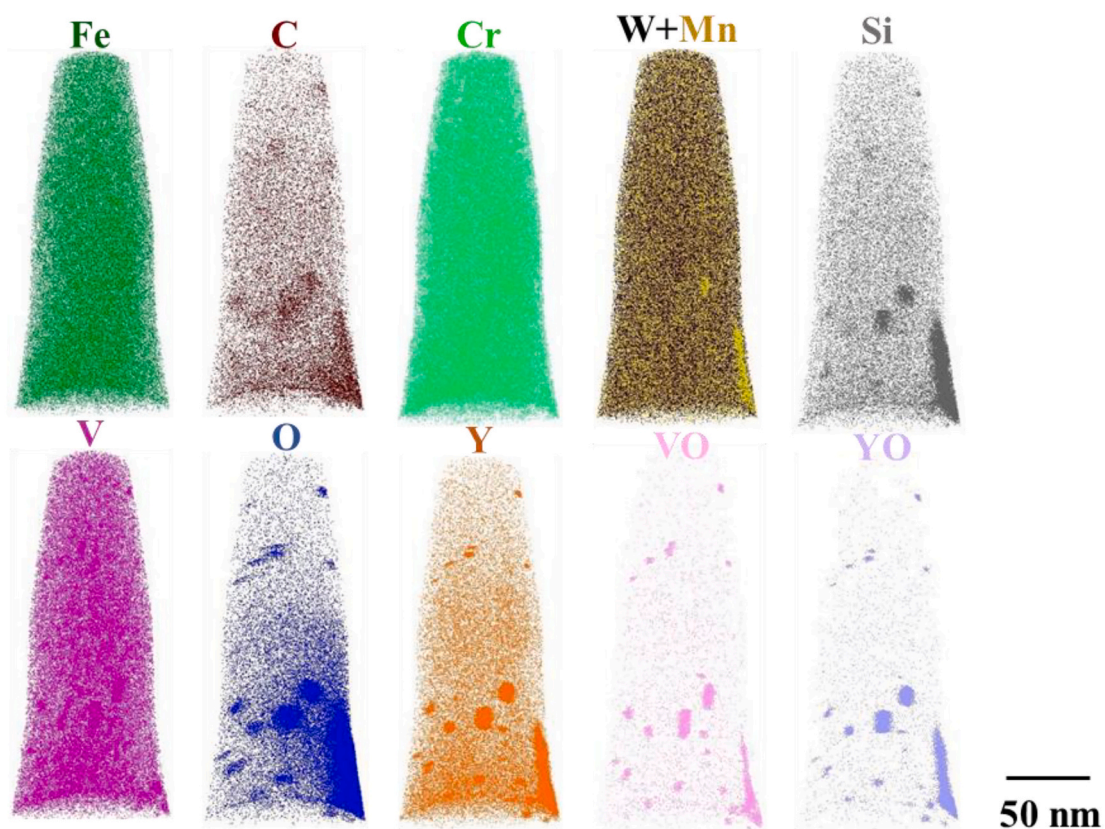
Fig. 4. Compositional maps of representative reconstructions of 0.3% Y_2O_3 ODS Eurofer samples (a) in the reference state and (b) annealed at 1400 K-FC.

oxide dispersion throughout the matrix, since much larger areas are analysed in comparison to APT. On the other hand, the measurement of the number density of oxide particles with TEM can be more challenging, because of the difficulty in determining the thickness of the samples and, thus, the analysed volume [19]. In the present work, the thickness of TEM samples was estimated to be of 100 nm.

Fig. 5(a) presents the particle size distributions measured with TEM and APT. In the reference condition, both techniques show that ~96% of the oxide nanoparticles have a diameter smaller than 8 nm, the remaining 4% have sizes up to 22 nm. For the annealed condition, the size distribution obtained with TEM is broader and shows coarsening of oxide nanoparticles, in which 78% of the particles with diameter smaller than 8 nm and 22% with sizes from 8 nm to 50 nm. The peak of the distribution calculated with TEM shifts from 3.7 ± 0.01 nm to 5.3 ± 0.04 nm with annealing at 1400 K. The same trend is observed with APT, with the peak of the distribution changing from 5.0 ± 0.1 nm in the reference state to 6.0 ± 0.1 nm in the annealed condition.

In Fig. 5(b) the number density of oxide particles determined with APT is shown, and corresponds to 2×10^{23} particles.m^{-3} in the reference state and 1.1×10^{23} particles.m^{-3} in the annealed condition. The decrease in number density is consistent with the particle coarsening discussed in Fig. 5(a). The number densities derived from TEM micrographs are one order of magnitude lower than the obtained with APT, and no difference between reference state and annealed condition could be seen. The reason for this discrepancy is related to the limitations associated with TEM, discussed previously. In particular for the reference state, the number density of particles calculated with TEM images is underestimated: the material was in a state of high deformation that strongly affected the contrast between the matrix and oxide nanoparticles (Fig. 3(b)).

The average chemical composition of all nanoparticles detected in the cluster analysis is given in Table 2. The main elements contained in the particles are Y, O, Cr and V. Overall, the average composition of the nanoparticles was not largely affected by the annealing treatment at 1400 K, except for a slight decrease in the V content. A possible relation between particle size and chemical composition was taken into account in our analysis, but no consistent correlation was encountered. In Fig. 6, elemental maps of the sample annealed at 1400 K, obtained with EDS-TEM, show the depletion of Fe inside the oxide nanoparticles, especially in the larger ones. Hirata et al. [4] also reported the depletion of Fe in Y-O based nanoparticles using STEM-EELS maps. The high Fe concentration measured with APT is related to ion trajectory aberrations during the APT measurements, discussed in [20–22]. In particular, Dhara et al. [22] observed a similar high Fe content in nano-sized Ti

precipitates, which, in principle, should also not contain Fe as main elemental component. It is not possible to conclude that the oxide nanoparticles present in the 0.3% Y$_2$O$_3$ ODS Eurofer steel do not contain a low content of Fe in their composition, but the high levels shown in Table 2 are not realistic. Williams et al. [21] discuss that the effect of trajectory aberrations is stronger in the smaller particles, which have dimensions similar to the size of the aberration (few nanometers) [21].

Fig. 6 confirms the Si-enrichment of large Y-O based nanoparticles, illustrated in Fig. 4, and suggests that some of these large particles are Cr-depleted in their cores. Multiple authors observed that Y-O based nanoparticles, present in different ODS steels, have a type of core-shell structure, with a Cr-rich shell and variable core composition [4,6,21,23–25]. Hence, the structure of the particles in the reference state and annealed samples was assessed by applying an isosurface of 1 atomic % Y on the APT data and by calculating proxigrams and concentration profiles of the particles. The results are presented in Fig. 7, which contains two indicative examples of particles per analysed condition. The software IVAS calculates proxigrams and concentrations profiles considering the presence of Fe, however, in order to better visualize the concentration curves of the other elements, Fe is removed from the plots. The proxigrams in Fig. 7(a) and (b), correspondent to particles in the reference state, show the increase in Cr concentration once the interface of the particle is crossed; the Cr concentration seems to achieve a plateau or decrease in the core of the particle. The concentration profiles in Fig. 7(a1) and (b1) show more clearly the decrease in Cr concentration inside the particle. This behaviour is considered to be indicative of a Cr-shell [6,21,23,24]. Still analysing the particles present in the reference condition, Figs. 7(a1) and (b1) show a core rich in Y, O, V and smaller concentrations of Si and Mn. The concentrations of W and C are extremely low in the particles and, therefore, are not considered to be part of the core. All analysed particles in the reference state exhibited a Cr-shell and the Cr concentration at the shell varied between ~10 atomic % to ~20 atomic %.

Figs. 7(c) and (d) show proxigrams calculated for representative particles present in the annealed state. In Fig. 7(c) the increase in Cr around the particle interface is clearly seen and its respective ROI concentration profile in Fig. 7(c1) confirms the Cr-shell structure. However, not all particles present in the annealed state exhibited the marked Cr-shell. Figs. 7(d) and (d1) show an example of particle in which the Cr concentration at the interface is not significantly higher than at the matrix, suggesting the formation of a thinner Cr-shell or its absence. The composition of particles cores in the annealed state is the same as in the reference condition, but some particles are Si and Mn-enriched (Fig. 7 (d1)), in agreement with Figs. 4(b) and 6. Finally, the particle analysed
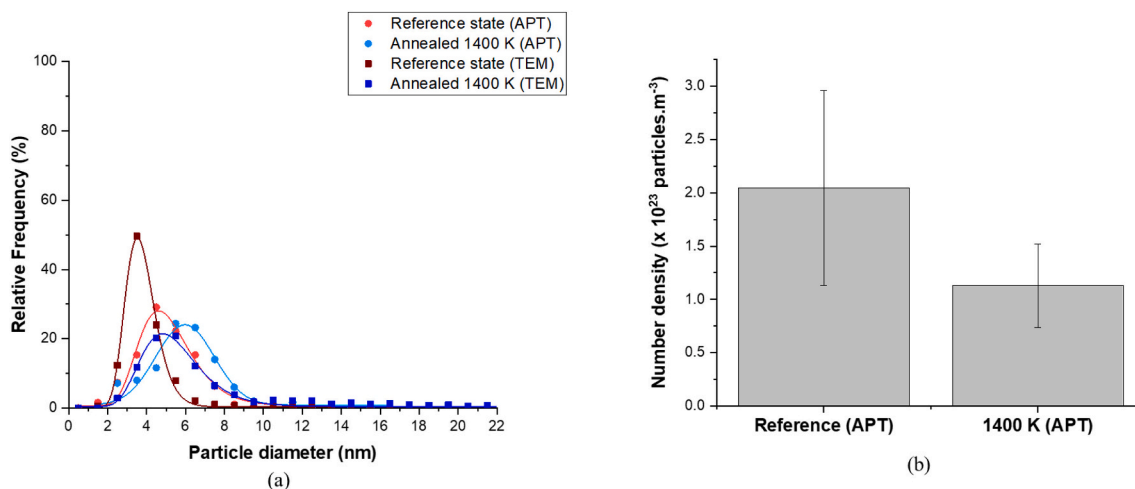

Fig. 5. (a) Particle size distributions and (b) number density of oxide nanoparticles calculated for the 0.3% Y$_2$O$_3$ ODS Eurofer steel in the reference state and annealed at 1400 K-FC, using TEM and APT.

Table 2
Average chemical composition of the oxide nanoparticles, in atomic percentage, determined by cluster analysis of APT data.

	C	Si	O	Cr	V	Fe	Mn	Y	W
Reference state	0.2 ± 0.8	0.4 ± 0.4	12.7 ± 4.8	12.5 ± 9.0	8.4 ± 5.7	44.8 ± 13.2	0.6 ± 0.5	19.1 ± 10.4	0.2 ± 0.4
Without Fe	0.3 ± 1.0	0.7 ± 0.7	23.0 ± 5.6	23.5 ± 13.0	15.4 ± 8.0	–	1.3 ± 1.0	33.7 ± 12.4	0.4 ± 0.6
Annealed 1400 K	0.3 ± 0.6	0.3 ± 0.3	10.3 ± 5.6	8.9 ± 2.4	5.0 ± 3.9	59.5 ± 11.2	0.6 ± 0.4	14.0 ± 6.3	0.3 ± 0.6
Without Fe	0.8 ± 0.9	0.8 ± 0.7	24.8 ± 6.9	23.8 ± 8.2	11.6 ± 5.3	–	1.6 ± 1.1	34.1 ± 6.9	0.8 ± 0.8
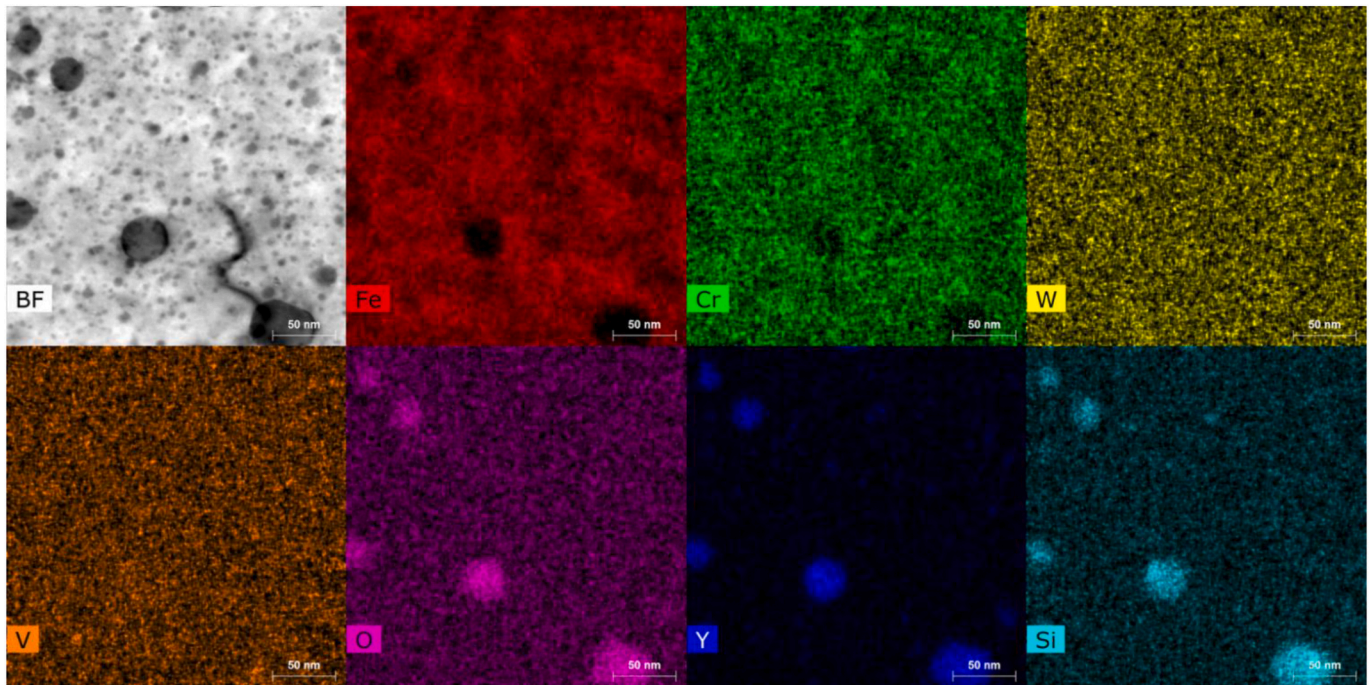
Fig. 6. Qualitative compositional maps of Y-O based nanoparticles of various sizes, present in the 0.3% Y_2O_3 ODS Eurofer steel annealed at 1400 K-FC.

in Figs. 7(d) and (d1) was located at the end of the APT tip and, for this reason, the average concentration at 10 nm is biased (low ion count number).

In Fig. 4(b) can be seen a large oxide nanoparticle present at the bottom right of the reconstruction, with size of ~60 nm and rich in O, Y and Si. To further investigate the structural composition of this large particle, isosurfaces of 1 atomic % O and 1 atomic % Y were applied. Fig. 8 shows in more detail the reconstructed particle with the 1 atomic % O and Y isosurfaces and the proxigrams calculated for these interfaces. The particle clearly has an outer layer rich in O, which also contain a Cr concentration slightly higher than the matrix (Fig. 8(b)). The core of the particle has high Y and O contents, a Cr content of ~8 atomic % (less than the observed for smaller particles), very low V concentration and higher levels of Si and Mn. These results agree with the qualitative composition of large particles (> 20 nm) obtained with the EDS-TEM elemental maps of Fig. 6.

3.2. Determination of Zener pinning force

The Zener pinning force originated by the Y-O based nanoparticles was determined for the reference state and annealed condition, using a modified Zener equation [26] that has been applied in the analysis of ODS steels [16,17].

$$F_Z = \frac{3}{8}\frac{\sigma f^{2/3}}{r} \tag{1}$$

Where F_z is the Zener pinning force, σ is the interfacial energy of grains present in the matrix, f is the volume fraction of oxide nanoparticles in the material and r is the radius of the oxide nanoparticles.

The volume fraction of oxide nanoparticles in the reference state and after annealing at 1400 K was calculated using the data obtained with APT cluster analysis, by dividing the total volume of oxide particles detected in a sample by the volume of the APT tip. The oxide nanoparticle radius was taken as the weighted average of each size distribution measured with TEM. For pinning of α/γ interface, $\sigma_{\alpha/\gamma} = 0.56$ J.m^{-2} [12]; for pinning of α/α boundaries, $\sigma_{\alpha/\alpha} = 0.32$ J.m^{-2} [27]. The parameters used and the resulting F_z are summarized in Table 3.

The results show the decrease of F_z with the increase of oxide nanoparticle size during annealing at 1400 K, and can be correlated to the overall coarser microstructure obtained after annealing at 1400 K (Fig. 2).

4. Discussion

4.1. Formation of the microstructure during annealing at 1400 K

The hypothesis raised in our previous work [11] to explain the microstructure of the 0.3% Y_2O_3 ODS Eurofer steel, obtained after annealing at 1400 K was based on the coarsening of oxide nanoparticles during the treatment. The hypothesis was that with coarsening, the Zener pinning force exerted by the particles become weaker, allowing a higher degree of grain growth. In the present work we examined the Y-O based nanoparticles in the reference condition and after annealing at 1400 K, using TEM and APT and found that, indeed, the particles undergo coarsening during the annealing treatment, which leads to the decrease of the Zener pinning force, F_z.

During annealing at 1400 K different processes have the potential to take place:
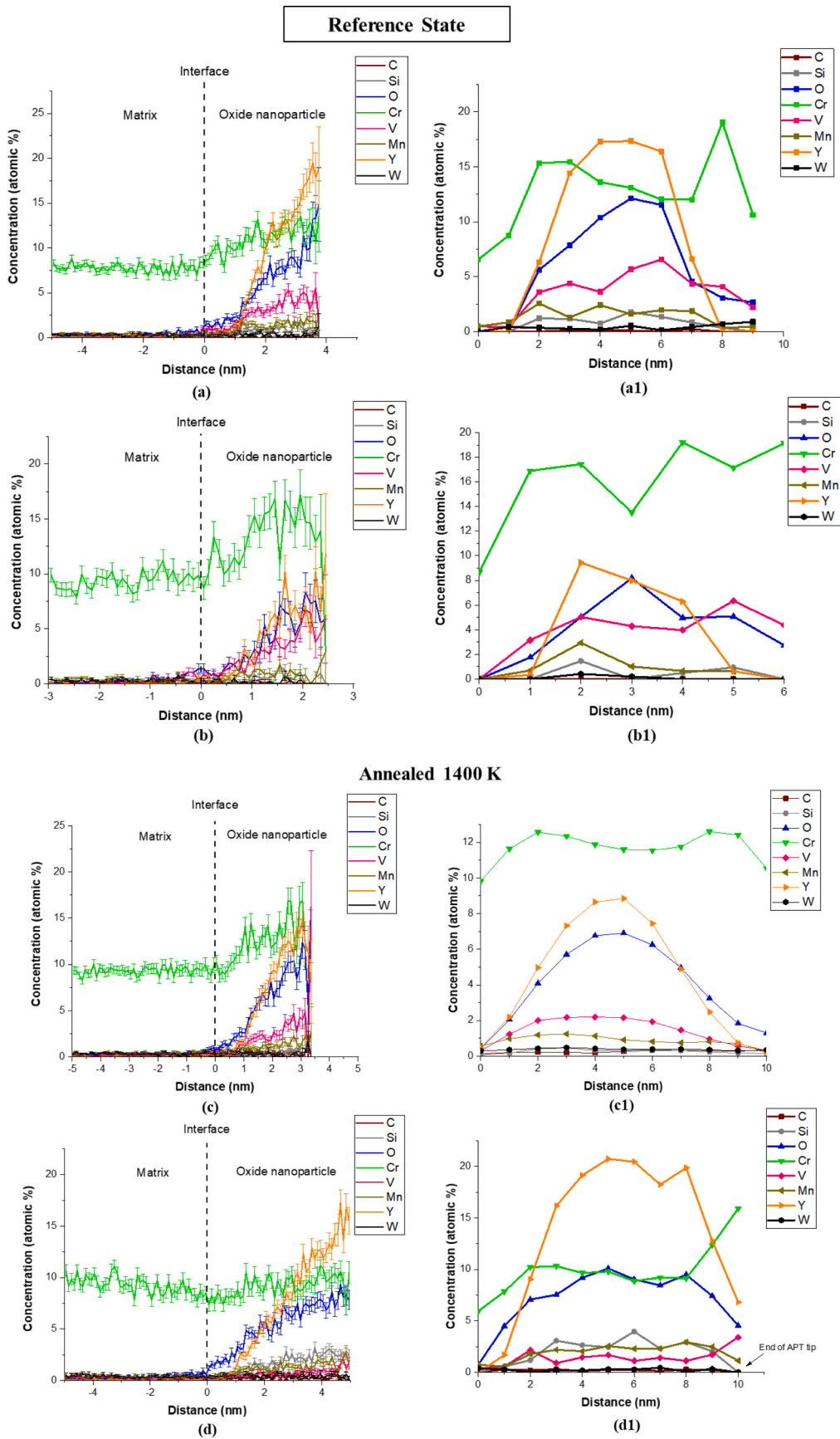
Fig. 7. (a),(a1) and (b), (b1) Proxigram along 1% Y isosurface and respective concentration profile along ROI of two representative oxide nanoparticles present in the reference state sample. (c),(c1) and (d),(d1) Proxigrams and concentration profiles along ROIs of two particles present in the sample annealed at 1400 K-FC.
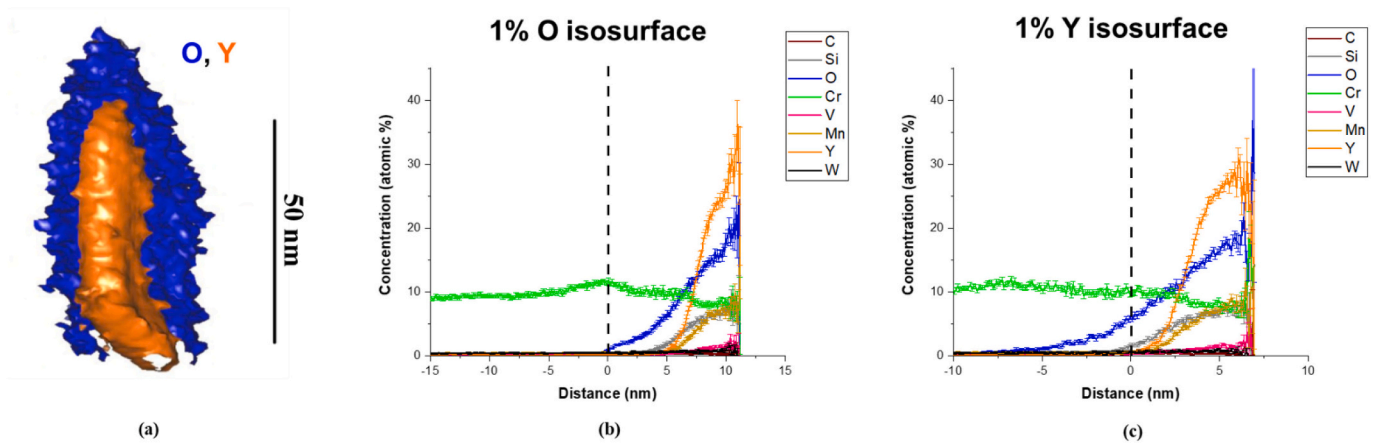
Fig. 8. (a) Detail of large Y-O nanoparticle present in the sample annealed at 1400 K-FC (shown previously in Fig. 3(b), at the bottom right of the reconstruction), with isosurfaces of 1% O and 1% Y applied. (b) and (c) are the correspondent proxigrams.

Table 3
Parameters used in the modified Zener equation [26] and Zener forces exerted on the α/γ and α/α interfaces.

| | F | r (nm) | $\sigma_{\alpha/\gamma} = 0.56$ J.m^{-2} | $\sigma_{\alpha/\alpha} = 0.32$ J.m^{-2} |
			$F_{z,\,\alpha/\gamma}$ (J.m^{-3})	$F_{z,\,\alpha/\alpha}$ (J.m^{-3})
Reference state	0.02	2.3	6.9×10^6	3.9×10^6
Annealed at 1400 K	0.02	4.2	3.4×10^6	2.0×10^6

(1) the (incomplete) transformation of ferrite into austenite,

(2) coarsening of the Y-O based nanoparticles, and.

(3) recrystallization of untransformed ferrite, due to its prior high deformation energy in the reference state.

Multiple studies [16–18] have shown with dilatometry and *in-situ* X-Ray Diffraction that ODS steels with ferritic/martensitic matrix do not undergo complete austenitization: a fraction of ferrite remains untransformed even at temperatures above A_{c3} and, upon cooling to room temperature, the retained ferrite grains can be seen dispersed in the martensitic matrix. The suggested reason is that the oxide nanoparticles dispersed in the matrix pin the α/γ interface, decreasing its velocity, and not allowing the complete consumption of the ferrite-parent phase [16,17]. The driving force for the austenitic transformation, $\Delta G_{\alpha/\gamma}$, in the 0.3% Y$_2$O$_3$ ODS Eurofer as a function of temperature has been estimated using Thermo-Calc 2018a, in order to qualitatively analyse its competition with $F_{Z,\,\alpha/\gamma}$, calculated in Section 3.2. $\Delta G_{\alpha/\gamma}$ was estimated by the difference between the formation energies of austenite and ferrite. This comparison of $F_{Z,\,\alpha/\gamma}$ to $\Delta G_{\alpha/\gamma}$ is considered qualitative because $F_{Z,\,\alpha/\gamma}$ will vary locally within the material, due to the heterogeneity in oxide nanoparticle size, and because the α/γ phase transformation involves other processes like nucleation and partitioning of solute elements. The estimated $\Delta G_{\alpha/\gamma}$ values are one order of magnitude higher than the $F_{Z,\,\alpha/\gamma}$ values presented in Table 3, with a maximum at 1300 K of approximately 1.6×10^7 J.m^{-3}, confirming that the oxide nanoparticles affect the kinetics of the transformation by an overall decrease in interface velocity, specially when they present a size distribution in the reference state. Another effect that might contribute to the hindering of the α/γ interface is the solute drag. Davis et al. [14] observed the segregation of W at grain boundaries of a 14YWT ODS steel, in its as-produced condition. In the 0.3% Y$_2$O$_3$ ODS Eurofer, with the dissolution of M$_{23}$C$_6$ precipitates, located preferentially at grain boundaries [11], the contents of C, Cr, V and W in the matrix are increased (Fig. 4). These elements could segregate or form clusters around the grain boundaries/interfaces and exert the so-called drag force, F_D. When the grain boundary or interface moves, it causes an increase on the energy state of the segregated/clustered solute, which, in

turn, will exert a force to pull the grain boundary back [28].

Since coarsening of the oxide nanoparticles likely involves the dissolution of smaller particles and diffusion of its elemental components towards larger ones, the process is not considered to occur instantaneously as the material reaches the annealing temperature of 1400 K. Thus, it is likely that in the beginning of the treatment, the average Zener pinning force exerted in the microstructure is higher than at its later stages. The average Vickers hardness measured for the sample annealed at 1400 K and water quenched is lower than in the reference state (Fig. 2). The coarse ferrite grains identified in this sample, indicated in Fig. 2(b), do not present the roughness seen in the reference state (Fig. 2(c)), and this is an indication of recrystallization. Because of the high cooling rate associated to the process of water quench, it is likely that partial recrystallization occurs at the later stages of the 1400 K annealing treatment, when F_z is decreased. During cooling inside the furnace, at a lower cooling rate, a higher fraction of recrystallized ferrite formed, as seen in Fig. 2(a).

4.2. Core/shell structure and chemical composition of oxide nanoparticles

With the APT analysis it was possible to determine the chemical composition of the oxide nanoparticles present in the 0.3% Y$_2$O$_3$ ODS Eurofer steel. Overall, the particles are formed by a Cr-rich shell and a core enriched in Y, O and V. The presence of a Cr-rich shell has been reported by several authors, either in ferritic and martensitic ODS steels [4,6,21,23–25,29]. Hirata et al. [4] suggested that the Cr-shell is responsible for the high coherency of the oxide nanoparticles with the ferritic matrix, possibly due to the similar BCC Cr and ferrite crystal structure. The high coherency with the matrix is one of the attributes that lower the driving force for particle coarsening, and, thus, is responsible for keeping the particles refined for long periods of time and at high temperatures. However, in martensitic steels, the high temperature phase transition of ferrite into austenite has been suggested to affect this coherency relation of the particle with the matrix [17]. This can partially explain the coarsening observed after annealing at 1400 K. It is interesting to point out that particles with diameter larger than 20 nm seem to be depleted in Cr (Fig. 5) and to have a thinner or absent Cr-shell (Fig. 8).

Other ODS Eurofer steel has shown higher thermal stability than the one here studied: oxide particle coarsening to an average size of 25 nm has been reported at temperatures above 1500 K [8]. In other ODS Eurofer steels [6,21,24], Ta has been detected in the core of the oxide nanoparticles. Fu et al. [24] reported the formation of finer oxide nanoparticles in ODS Eurofer containing higher Ta and V contents. The same authors [24] have also observed that, when the Ta content is increased, the V once present in the core of oxide nanoparticles is

expelled to the Cr-shell and they attribute this behaviour to the higher affinity of Ta with O, in comparison to Cr and V [24]. The absence of Ta in the 0.3% Y_2O_3 ODS Eurofer steel could be related to the lower thermal stability of the oxide nanoparticles, but more investigations are necessary to verify this possible relation.

5. Conclusions

In the present work, the effect of annealing at 1400 K on the microstructure and oxide nanoparticles in a 0.3% Y_2O_3 ODS Eurofer steel was evaluated, using TEM and APT. The results obtained showed that:

(i) The oxide nanoparticles go through coarsening during the annealing treatment and have their average particle diameter increased from 3.7 ± 0.01 nm (reference state) to 5.3 ± 0.04 nm;

(ii) With coarsening, the Zener pinning force exerted by the oxide nanoparticles was decreased, leading to the formation of a coarser microstructure, in comparison to the one in the reference state, composed of recrystallized ferrite and martensite;

(iii) The analysis of the microstructure and Vickers hardness of the material in the reference state, annealed at 1400 K followed by furnace cooling and annealed at 1400 K and water quenched indicates that ferrite retained above Ac_3 recrystallizes at 1400 K, due to the decrease of the overall Zener pinning force. When the material is cooled inside the furnace, part of the ferrite recrystallizes during cooling;

(iv) The oxide nanoparticles have a well-known core-shell structure, in which the core is rich in Y, O and V and the shell is enriched in Cr. The average composition of the particles does not change significantly after annealing at 1400 K, except for a slight decrease in the Cr and V contents.

Credit author statement

Viviam Marques Pereira: conceptualization, methodology, validation, formal analysis, investigation, resources, data curation, writing – original draft, writing – review and editing.

Thomas Davis: methodology, formal analysis, resources, writing – review and editing.

Mercedes Mayoral Hernandez: methodology, formal analysis, resources, writing – review and editing.

Ankit Kumar: methodology, formal analysis, resources, writing – review and editing.

Henk Schut: term, conceptualization, validation, formal analysis, investigation, resources, writing – review and editing, supervision.

Jilt Sietsma: term, conceptualization, validation, writing – review and editing, supervision, project administration.

Data availability

The raw data required to reproduce these findings is available to download.

Declaration of Competing Interest

The authors declare that they have no competing financial interests or personal relationships that could have appeared to influence the work reported in this paper.

Acknowledgements

References

[1] S.J. Zinkle, et al., Development of next generation tempered and ODS reduced activation ferritic/martensitic steels for fusion energy applications, Nucl. Fusion 57 (9) (2017), https://doi.org/10.1088/1741-4326/57/9/092005.

[2] T.P. Davis, Review of the iron-Based Materials Applicable for the Fuel and Core of Future Sodium Fast Reactors, 2018.

[3] G.R. Odette, Recent progress in developing and qualifying nanostructured ferritic alloys for advanced fission and fusion applications, Jom 66 (12) (2014) 2427–2441, https://doi.org/10.1007/s11837-014-1207-5.

[4] A. Hirata, T. Fujita, Y.R. Wen, J.H. Schneibel, C.T. Liu, M.W. Chen, Atomic structure of nanoclusters in oxide-dispersion-strengthened steels, Nat. Mater. 10 (12) (2011) 922–926, https://doi.org/10.1038/nmat3150.

[5] S. Ukai, S. Mizuta, M. Fujiwara, T. Okuda, T. Kobayashi, Development of 9cr-ods martensitic steel claddings for fuel pins by means of ferrite to austenite phase transformation, J. Nucl. Sci. Technol. 39 (7) (2002) 778–788, https://doi.org/10.1080/18811248.2002.9715260.

[6] K.D. Zilnyk, K.G. Pradeep, P. Choi, H.R.Z. Sandim, D. Raabe, Long-term thermal stability of nanoclusters in ODS-Eurofer steel: an atom probe tomography study, J. Nucl. Mater. 492 (2017) 142–147, https://doi.org/10.1016/j.jnucmat.2017.05.027.

[7] C. Cayron, E. Rath, I. Chu, S. Launois, Microstructural evolution of Y2O3 and MgAl 2O4 ODS EUROFER steels during their elaboration by mechanical milling and hot isostatic pressing, J. Nucl. Mater. 335 (1) (2004) 83–102, https://doi.org/10.1016/j.jnucmat.2004.06.010.

[8] M.J.R. Sandim, I.R. Souza Filho, E.H. Bredda, A. Kostka, D. Raabe, H.R.Z. Sandim, Coarsening of Y-rich oxide particles in 9%Cr-ODS Eurofer steel annealed at 1350 °C, J. Nucl. Mater. 484 (2017) 283–287, https://doi.org/10.1016/j.jnucmat.2016.12.025.

[9] R.A. Renzetti, H.R.Z. Sandim, M.J.R. Sandim, A.D. Santos, A. Möslang, D. Raabe, Annealing effects on microstructure and coercive field of ferritic-martensitic ODS Eurofer steel, Mater. Sci. Eng. A 528 (3) (2011) 1442–1447, https://doi.org/10.1016/j.msea.2010.10.051.

[10] M.A. Moghadasi, M. Nili-Ahmadabadi, F. Forghani, H.S. Kim, Development of an oxide-dispersion-strengthened steel by introducing oxygen carrier compound into the melt aided by a general thermodynamic model, Sci. Rep. 6 (November) (2016) 1–10, https://doi.org/10.1038/srep38621.

[11] V.S.M. Pereira, H. Schut, J. Sietsma, A study of the microstructural stability and defect evolution in an ODS Eurofer steel by means of electron microscopy and positron annihilation spectroscopy, J. Nucl. Mater. 540 (2020), https://doi.org/10.1016/j.jnucmat.2020.152398.

[12] K.D. Zilnyk, V.B. Oliveira, H.R.Z. Sandim, A. Möslang, D. Raabe, Martensitic transformation in Eurofer-97 and ODS-Eurofer steels: a comparative study, J. Nucl. Mater. 462 (2015) 360–367, https://doi.org/10.1016/j.jnucmat.2014.12.112.

[13] T.L. Martin, et al., Comparing the consistency of atom probe tomography measurements of small-scale segregation and clustering between the LEAP 3000 and LEAP 5000 instruments, Microsc. Microanal. 23 (2) (2017) 227–237, https://doi.org/10.1017/S1431927617000356.

[14] T.P. Davis, et al., Electron microscopy and atom probe tomography of nanoindentation deformation in oxide dispersion strengthened steels, Mater. Charact. 167, no. April (2020) 110477, https://doi.org/10.1016/j.matchar.2020.110477.

[15] D. Vaumousse, A. Cerezo, P.J. Warren, A procedure for quantification of precipitate microstructures from three-dimensional atom probe data, Ultramicroscopy 95 (SUPPL) (2003) 215–221, https://doi.org/10.1016/S0304-3991(02)00319-4.

[16] M. Yamamoto, S. Ukai, S. Hayashi, T. Kaito, S. Ohtsuka, Formation of residual ferrite in 9Cr-ODS ferritic steels, Mater. Sci. Eng. A 527 (16–17) (2010) 4418–4423, https://doi.org/10.1016/j.msea.2010.03.079.

[17] M. Yamamoto, S. Ukai, S. Hayashi, T. Kaito, S. Ohtsuka, Reverse phase transformation from α to γ in 9Cr-ODS ferritic steels, J. Nucl. Mater. 417 (1–3) (2011) 237–240, https://doi.org/10.1016/j.jnucmat.2010.12.250.

[18] A. Durand, et al., Characterization of untransformed ferrite in 10Cr and 12Cr ODS steels, Materialia 16 (2021), 101066, https://doi.org/10.1016/j.mtla.2021.101066.

[19] D.J. Larson, B. Gault, B.P. Geiser, F. De Geuser, F. Vurpillot, Atom probe tomography spatial reconstruction: status and directions, Curr. Opin. Solid State Mater. Sci. 17 (5) (2013) 236–247, https://doi.org/10.1016/j.cossms.2013.09.002.

[20] T.P. Davis, et al., Materialia atom probe characterisation of segregation driven Cu and Mn – Ni – Si co-precipitation in neutron irradiated T91 tempered-martensitic steel, Materialia 14 (October) (2020), https://doi.org/10.1016/j.mtla.2020.100946.

[21] C.A. Williams, E.A. Marquis, A. Cerezo, G.D.W. Smith, Nanoscale characterisation of ODS-Eurofer 97 steel: an atom-probe tomography study, J. Nucl. Mater. 400 (1) (2010) 37–45, https://doi.org/10.1016/j.jnucmat.2010.02.007.

[22] S. Dhara, R.K.W. Marceau, K. Wood, T. Dorin, Data in Brief Atom probe tomography data analysis procedure for precipitate and cluster identi fi cation in a Ti-Mo steel, Data Br. 18 (2018) 968–982, https://doi.org/10.1016/j.dib.2018.03.094.

[23] A.J. London, et al., Comparison of atom probe tomography and transmission electron microscopy analysis of oxide dispersion strengthened steels, J. Phys. Conf. Ser. 522 (1) (2014), https://doi.org/10.1088/1742-6596/522/1/012028.

[24] J. Fu, T.P. Davis, A. Kumar, I.M. Richardson, M.J.M. Hermans, Characterisation of the influence of vanadium and tantalum on yttrium-based nano-oxides in ODS Eurofer steel, Mater. Charact. 175 (April) (2021), https://doi.org/10.1016/j.matchar.2021.111072.

[25] V. De Castro, E.A. Marquis, S. Lozano-Perez, R. Pareja, M.L. Jenkins, Stability of nanoscale secondary phases in an oxide dispersion strengthened Fe-12Cr alloy, Acta Mater. 59 (10) (2011) 3927–3936, https://doi.org/10.1016/j.actamat.2011.03.017.

[26] T. Nishizawa, I. Ohnuma, K. Ishida, Examination of the Zener relationship between grain size and particle dispersion, Mater. Trans. JIM 38 (11) (1997) 950–956.

[27] T. Nagano, M. Enomoto, Calculation of the interfacial energies between α and γ iron and equilibrium particle shape, Metall. Mater. Trans. A 37 (3) (2006) 929–937, https://doi.org/10.1007/s11661-006-0066-2.

[28] V.K. Devra, J. Maity, Solute drag effect on austenite grain growth in hypoeutectoid steel, Philos. Mag. Lett. 100 (6) (2020) 245–259, https://doi.org/10.1080/09500839.2020.1750723.

[29] K.H. Hong, J.B. Seol, J.H. Kim, First principles determination of formation of a Cr shell on the interface between Y–Ti–O nanoparticles and a ferritic steel matrix, Appl. Surf. Sci. 481 (March) (2019) 69–74, https://doi.org/10.1016/j.apsusc.2019.03.081.